Experimental testing of ab initio potential energy surfaces: Stereodynamics of NO($A^2\Sigma^+$) + Ne inelastic scattering at multiple collision energies

Experimental testing of ab initio potential energy surfaces: Stereodynamics of NO($A^2\Sigma^+$) + Ne inelastic scattering at multiple collision energies

Thomas F. M. Luxford,[1] Thomas R. Sharples,[1] Kenneth G. McKendrick[1] and Matthew. L. Costen[1,a]

[1]*Institute of Chemical Sciences, Heriot-Watt University, Edinburgh, EH14 4AS, U. K.*

ABSTRACT

We present a crossed molecular beam velocity-map ion imaging study of state-to-state rotational energy transfer of NO($A^2\Sigma^+$, v = 0, $N = 0$, $j = 0.5$) in collisions with Ne atoms. From these measurements, we report differential cross sections and angle-resolved rotational angular momentum alignment moments for product states $N' = 3$, 5-10 for collisions at an average energy of 523 cm^{-1}, and $N' = 3$, 5-14 for collisions at an average energy of 1309 cm^{-1}, respectively. The experimental results are compared to the results of close-coupled quantum scattering calculations on two literature *ab initio* potential energy surfaces (PESs) (Pajón-Suárez *et al.*, Chem. Phys. Lett. **429**, 389 (2006), and Cybulski and Fernández, J. Phys. Chem. A. **116**, 7319 (2012)). The differential cross sections from both experiment and theory show clear rotational rainbow structures at both collision energies, and comparison of the angles observed for the rainbow peaks leads to the conclusion that Cybulski and Fernández PES better represents the NO($A^2\Sigma^+$)-Ne interaction at the collision energies used here. Sharp, forward scattered (< 10°), peaks are observed in the experimental differential cross sections for a wide range of N' at both collision energies, which are not reproduced by theory on either PES. We identify these as *L*-type rainbows, characteristic of attractive interactions, and consistent with a shallow well in the collinear Ne-N-O geometry, similar to that calculated for the NO($A^2\Sigma^+$)-Ar surface (Kłos *et al*., J. Chem. Phys. **129**, 244303 (2008)), but absent from both of the NO($A^2\Sigma^+$)-Ne surfaces tested here. The angle-resolved alignment moments calculated by quantum scattering theory are generally in good agreement with the experimental results, but both experiment and quantum scattering theory are dramatically different to the predictions of a classical rigid-shell, kinematic-apse conservation, model. Strong oscillations are resolved in the experimental alignment moments as a function of scattering angle, confirming and extending the preliminary report of this behavior (Steill *et al.*, J Phys Chem A. **117**, 8163 (2013)). These oscillations are correlated with structure in the differential cross section, suggesting an interference effect is responsible for their appearance.

I. INTRODUCTION

Inelastic collisions are ubiquitous in the gas phase, and play a primary role in the redistribution of energy in almost all gas-phase systems of practical interest. Understanding and predicting these interactions requires, within the Born-Oppenheimer approximation, a knowledge of the *ab initio* potential energy surface (PES) that describes the forces acting

[a] Author to whom correspondence should be addressed. Electronic mail: m.l.costen@hw.ac.uk

between the collision partners. Small-molecule systems, in particular those involving molecular free radical species, are of special significance. Not only are they often amenable to detailed, state-resolved, experimental study, but they also typically play a central role in the chemistry of important gas-phase environments, including planetary atmospheres, combustion systems and technological plasmas.[1, 2] The diatomic radicals; OH, CH, CN, and in particular NO, have been the targets of particularly intensive study, as their small electron number allows high-level electronic structure theory to be applied, while their open-shell character provides a challenge to theory. Experiment and theory can then complement one another. Experiments test the predictions of calculations, either quasi-classical trajectory (QCT) or quantum scattering (QS), on the *ab initio* PES. Using exact QS calculations, disagreements between theory and experiment ideally provide information on what aspect of the PES requires improvement. Scattering calculations provide additional insight into the dynamics of the collision process, helping to establish more widely applicable approximate models of inelastic collisions. In this paper we use state-of-the-art measurements of the stereodynamics of rotational energy transfer (RET) in NO($A^2\Sigma^+$) + Ne collisions to test and compare two recent *ab initio* NO(A)-Ne PESs, and provide suggestions for possible improvements.

Until quite recently, the most widely used experimental test of PESs in inelastic scattering has been the measurement of state-to-state integral cross sections or rate constants.[3, 4] Such experiments have reached great sophistication with, for example, the use of Stark decelerators to exercise precise control over the collision energy, enabling state-to-state integral cross section measurements that explore the effect of the sequential energetic opening of rotational and fine-structure product channels.[5-9] High-resolution measurements of this type provide a very good test of the accuracy of the PES within the collision energy range; if good agreement is seen between experiment and full quantum scattering calculations on an *ab initio* PES, the calculated PES is likely to be correct. However, when disagreement is found, it is difficult to determine where the deficiencies in the PES lie, as most of the information about the chemical shape of the system has been lost in the averaging over initial and final collision properties inherent in a scalar measurement. Much more information about the shape of the PES, and hence more stringent and more informative testing, can be achieved with vector measurements.[10]

Whilst substantive information about the PES is available through measurements of the *j-j′* correlation,[11-13] it is generally the case that measurements of the differential cross section (DCS), i.e. *k-k′* correlation, and of the product rotational angular momentum polarization as a function of scattering angle, i.e. *k-k′-j′* correlation, provide the most detailed tests of the PES, and the most direct insight into its chemical shape. The current state-of-the-art method for determining DCSs in inelastic scattering is the combination of crossed molecular beams (CMB) with resonant laser ionization of the products (REMPI) and subsequent velocity-map imaging (VMI) of the resultant ions. This approach has been used to test a wide range of systems,[14-20] but the most intensively studied are those involving NO($X^2\Pi$) colliding with the rare gases, reflecting the easy handling of

the stable NO radical and its convenient spectroscopy.[21-36] The majority of these experimental studies on NO(X) + rare gases tested only a single *ab initio* version of the PES; however, the sensitivity of these stereodynamical measurements to the form of the PES is best illustrated by comparison to QS calculations on alternative versions of the *ab initio* PES. An early example is the work of Suzuki *et al.*, who tested NO(X)-Ar PESs calculated using two different electronic structure approaches, and found better agreement with experiment with the more recent, and higher level of theory PES.[21] A very recent example comes from the work of van de Meerakker and co-workers, who have performed experiments on NO(X)-Ar using a Stark decelerator to provide very high resolution in collision energy and angular scattering.[33, 34, 36] As a result, they have been able to resolve forward scattered diffraction oscillations in the DCS, and have shown that very subtle changes in the long-range region of the PESs may be identified as responsible for variations in the level of agreement of theory with specific features of the diffraction oscillations.[36]

All of the systems discussed above involved the ground electronic states of the radical species. We have recently demonstrated that it is possible to integrate a pulsed laser excitation step into a CMB-VMI experiment prior to collision, and hence apply this powerful technique to the stereodynamics of collisions of electronically excited radicals.[37-41] The spectroscopic selection of the excitation step prepares a single initial rotational level, and also introduces a well-defined start time to the collision process, simplifying the subsequent image analysis. In collisions of NO(A) + Ar, we have shown through comparison of the experimental DCS and predictions from QS calculations, that we are able to identify specific aspects of the *ab initio* PES that required improvement.[40] Most recently, we have shown quantitative agreement between experiment and theory in NO(A) + He scattering, and have used that to inform the interpretation of experimental results in the kinematically identical NO(A)-D_2 system, yielding predictions about the form of the hitherto unknown NO(A)-D_2 PES.[41] In most of these experiments, we have also measured the scattering angle-resolved rotational angular momentum moments. In both the NO(A)-Ar and NO(A)-He systems we see moments in good agreement with the QS calculations, but that disagree with classical hard-shell scattering models, in strong contrast to the majority of NO(X) + Rg scattering experiments.[23, 26-28] In preliminary experiments, performed in collaboration with the group of Chandler at Sandia National Laboratory, we also observed unusual angular momentum polarization in NO(A) + Ne scattering, including rapid oscillations in the polarization as a function of scattering angle.[39] In this paper, we present a comprehensive, systematic study of rotationally inelastic scattering of NO($A^2\Sigma^+$, v = 0, N = 0, j = 0.5) with Ne using our excited-state CMB-VMI technique. We determine DCSs and scattering angle resolved alignment moments for a wide range of product states at two distinct average collision energies, $\langle E_{col} \rangle$. At the lower energy, $\langle E_{col} \rangle$ = 523 cm^{-1}, we detect N' = 3 & 5-10, and at the higher energy, $\langle E_{col} \rangle$ = 1309 cm^{-1}, we detect N' = 3 & 5-14. We compare these to the results of collision-energy averaged QS calculations on two literature *ab initio*

PESs,[42, 43] identifying which is more accurate overall, and also suggest specific features of the PESs which require improvement.

II. METHODS

A. Experiment

The apparatus and the procedure used to carry out these experiments have been described in detail in previous publications, and only the essential details are given here.[40, 41] The NO and Ne colliders were separately expanded in pulsed molecular beams which intersected at 90° in a high vacuum chamber. For the low energy collisions, the NO (99.5%, BOC) was seeded in Ar (99.998%, BOC) at 10% concentration with a backing pressure of 3 bar, to give a Gaussian velocity distribution with a mean of 623 ms^{-1}, and full width at half maximum (FWHM) of 53 ms^{-1}. For the high energy collisions, NO was seeded in He (99.999%, BOC) at 10% concentration with a backing pressure of 3 bar, to give a mean velocity of 1398 ms^{-1} and FWHM of 91 ms^{-1}. In both cases, the second molecular beam contained neat Ne (99.999%, BOC) with a backing pressure of 5 bar, which gave a mean velocity of 809 ms^{-1} and FWHM of 54 ms^{-1}. These conditions resulted in Gaussian distributions of center-of-mass collision energies, E_{col}, with a mean of 523 cm^{-1} and FWHM of 57 cm^{-1} for the low-energy collisions, and a mean of 1309 cm^{-1} and FWHM of 137 cm^{-1} for the high-energy collisions, respectively. The methods used to measure the velocity distribution of the molecular beams are described in the Supplementary Material.

NO ($A^2\Sigma^+$, v = 0, N = 0, j = 0.5) was prepared in the crossing region of the molecular beams by excitation of NO($X^2\Pi$) via the $Q_1(0.5)$ transition of the A-X(0,0) band, using the output of a Nd:YAG pumped dye laser (Sirah CTSG / Continuum Surelite II-10) at 226.18 nm. The laser beam was unfocussed, with a fluence of 0.65 mJ cm^{-2} and a diameter of 2 mm for the low energy experiments, and 1.5 mm for the high-energy experiments, respectively. The inelastically scattered NO(A, v = 0, N') was probed after a 400 ns delay using a (1 + 1′) REMPI scheme. The NO(A) was first state-selectively excited to the $E^2\Sigma^+$ state via individual rotational transitions in the R branch of the E-A(0,0) band around 600 nm, using a Nd:YAG pumped dye laser (Sirah CSTR-DA24 / Continuum Surelite I-10). The resulting NO(E) was subsequently ionized at 532 nm using light from the same Nd:YAG laser. The spin-rotation splitting in the E-A(0,0) band is much smaller than the Doppler width of the transitions and hence the 600 nm probe light probes the two NO(A) $j' = N' \pm ½$ spin-rotation states for each N' equally. However, the loss of resolution of these two spin-rotation states does not limit the experimental insight into the scattering dynamics, since the electron spin can be considered a spectator during the collisions to a very good approximation.[12, 44] The polarization of the 600 nm probe laser beam was controlled using a photo-elastic modulator (PEM-90, Hinds Inc.), so that the electric vector was polarized horizontally (H) or vertically (V) in the lab frame, respectively in and perpendicular to the plane

of the molecular beams, providing sensitivity to the polarization of the product rotational angular momentum, N'. As described in our previous work, two saturating 532 nm ionization beams were used, arranged to maintain their polarizations orthogonal to one another and to the probe beam polarization, thereby minimizing any polarization sensitivity in the ionization step.[40, 41] The 600 nm beam and both of the 532 nm laser beams were unfocussed and were set to diameters of 3 mm. The fluence of the probe laser was set to 0.65 μJ cm^{-2} and that for each ionization laser beam was varied in the range 4-40 mJ cm^{-2} for different final N', with the higher fluences used for the high-N' states with smaller scattering cross sections. For the highest N' detected, $N' = 10$ at $\langle E_{col} \rangle$ =523 cm^{-1} and $N' = 14$ at $\langle E_{col} \rangle$ =1309 cm^{-1}, calculations (*vide infra*) predicted integral cross sections of 0.72 Å^2 and 0.46 Å^2, respectively. This is around the limit for the current apparatus for which probe-polarization-dependent images can be collected with adequate signal-to-noise. At both collision energies, and consistent with our previous measurements of collisions with Ar, He, and D_2, we do not report results for $N' = 1$, 2 or 4.[40, 41] The measurement of NO scattered into these final states is subject to interference from NO directly excited from the ground state by the spectral wing of the 226.18 nm state-preparation pulse. Although the state-preparation laser is directly resonant with only the desired $Q_1(0.5)$ transition, the necessary saturation of this transition results in the nearby bandhead structure of the Q_1 branch being overlapped by the far wing of the laser spectral bandwidth. NO is excited from the initial states NO(X, v = 0, F_1, j = 1.5, 2.5 and 4.5) on the $Q_1(1.5)$, $Q_1(2.5)$ and $Q_1(4.5)$ transitions, respectively. This results in intense signals at the NO beam velocity ('beam spots') in images acquired for $N' = 1$, 2 or 4. In principle, these interfering signals could be removed through background subtraction of images acquired without the collider beam. Indeed, the combination of low populations in these initial levels arising from the molecular beam cooling of the NO(X), and the off-resonance excitation, results in very small populations in $N = 1$, 2, or 4, compared to that in the desired $N = 0$ initial level. However, the total fraction of the $N = 0$ population scattered into different product-N' is also very small. As a result, the background signals are comparable in size to the scattering signal, and for the strongly forward scattered low-ΔN these beam spots appear in the same region of the image. We have been unable to measure accurately the total population removal fraction from $N = 0$, but based on the total inelastic collision cross section from QS calculations and estimates of the Ne collider beam density, we estimate that < 0.5% of the initially prepared $N = 0$ population undergoes inelastic scattering in the 400 ns time window. Since the fractional inelastic cross sections from $N = 0$ to $N' = 1$, 2 or 4 are ≈ 10% of the total, we estimate that the initial population prepared in the $N = 1$, 2 and 4 is < 0.05% of that prepared in $N = 0$. This compares well, for example, to the < 1% of initial population in different levels estimated by Stolte and co-workers in their hexapole state-selected NO(X) inelastic scattering experiments. This justifies our description of the experimental scattering as state-to-state, and our assumption in the QS calculations that all scattering originates in the $N' = 0$ state.[23]

The resulting NO^+ ions were velocity mapped onto a micro-channel plate (MCP) detector coupled to a phosphor screen (Photonis, 40 mm active diameter, P47 phosphor), with the light emitted from the phosphor recorded using a camera (Basler scA780-54fm, 782 × 582 pixel array). The voltage applied to the MCP plates was pulsed (120 ns pulse width) to discriminate against NO^+ ions arising from (1 + 1) REMPI by the pump laser, exploiting the 400 ns interval between the creation of these ions and the probing of the scattered NO(A). Scattering and background camera frames for the H and V geometries were acquired in batches of 200 laser shots in an interleaved fashion, and were subsequently summed in the data acquisition computer. For the background images the Ne molecular beam was delayed by 1 ms with respect to the NO beam. In order to avoid velocity-dependent detection efficiency arising from Doppler selection, the wavelength of the probe laser was scanned three times over the peak of the E-A transition in steps of 5 x 10^{-4} nm, with 16 steps being taken on each scan for the low-energy measurements, and 18 steps taken for the high-energy measurements. In total, 8 independent measurements were made for each final N' state across multiple days, with each low-energy measurement comprising 38,400 shots and each high-energy measurement comprising 43,200 shots.

B. Theory

The DCS and scattering angle-dependent alignment moments have been calculated in time-independent close-coupled quantum scattering (QS) calculations using the Hibridon suite of programs.[45] Scattering calculations were performed employing two literature PESs for the NO(A) + Ne system; the 2006 PES of Pajón-Suárez *et al.*, henceforth referred to as the PRRH PES,[42] and the 2012 PES of Cybulski and Fernández, henceforth referred to as the CF PES.[43] Both PESs were calculated with the NO bond length fixed at the A-state equilibrium value of 1.06 Å. For QS calculations using the Hibridon codes, the PESs must be expressed in the conventional form:

$$V(R,\alpha) = \sum_{l=0}^{M} f_l(R) P_l(\cos\alpha) \tag{1}$$

where R is the distance from the Ne atom to the NO center of mass, and α is the angle between $\boldsymbol{R}$ and the NO bond axis, with $\alpha = 0°$ corresponding to the O-N-Ne linear geometry. The R-dependent coefficients $f_l(R)$ are parameterized from individual electronic structure calculations performed for various values of R at fixed values of α. The PRRH PES was already available in this form,[45] while the CF PES was reparametrized from the functional form provided in the original publication.[43]

The NO(A) molecule was treated as a rigid rotor with rotational constants B = 1.987 cm^{-1} and γ = -0.0027 cm^{-1}.[46] For both potentials, calculations were performed at individual energies selected from within either of the two experimental collision energy distributions. For calculations in the $\langle E_{col} \rangle$ = 523 cm^{-1} distribution, a rotational basis up to N = 18 was

employed, with partial waves up to J_{tot} = 450.5 and propagation from 3 to 300 Bohr. For calculations in the $<E_{col}>$ = 1309 cm^{-1} distribution, a rotational basis up to N = 29 was employed, with partial waves up to J_{tot} = 600.5 and propagation from 3 to 300 Bohr. The calculations treated NO(A) as open shell and yielded DCSs for individual final spin-rotation levels $j' = N' \pm$ ½, which were summed to give the DCSs for formation of individual N', with the polarization moments for each N' obtained as the DCS-weighted average of the values for the two corresponding j' levels.

Calculations were performed at individual energies spanning a range of ± 3 standard deviations of the experimentally determined collision energy distributions around the mean collision energy, and the results averaged over the appropriate Gaussian collision energy distributions. On the PRRH PES, calculations were performed at 19 individual energies spaced by 8 cm^{-1} for $<E_{col}>$ = 523 cm^{-1}, and at 17 individual energies spaced by 21 cm^{-1} for $<E_{col}>$ = 1309 cm^{-1}. On the CF PES, calculations were performed at 17 individual energies spaced by 10 cm^{-1} for $<E_{col}>$ = 523 cm^{-1}, and at 19 individual energies spaced by 20 cm^{-1} for $<E_{col}>$ = 1309 cm^{-1}.

Neon has two major isotopes (^{20}Ne and ^{22}Ne, in the ratio ~10:1) and the slightly different masses result in different kinematics for collisions with the two isotopes. Due to the experimental spread in collision energies, scattering from the two isotopes is unresolved in the measured images. As discussed in the section II.C, the fitting procedure took into account the effect of the kinematics on the appearance of the images, while assuming that a single DCS and set of alignment moments described scattering from both colliders. Scattering calculations on the CF PES for a limited range of collision energies and using the reduced mass appropriate for the ^{22}Ne (12.689 amu) indicated only small changes in the DCS and alignment moments compared to those calculated for the ^{20}Ne isotope. Once averaged across the isotope ratio, the DCS and alignment moments showed negligible variation from the pure ^{20}Ne results compared to both the observed experimental errors, and the differences obtained from the two PESs. Consequently, all of the QS calculations reported in this paper were performed with a reduced mass of 11.977 amu, corresponding to collisions of NO(A) with the majority ^{20}Ne isotope.

Calculations of the scattering angle-dependent alignment moments have also been carried out using the kinematic apse (KA)[47] model discussed in previous publications.[39, 40] This model considers classical, impulsive scattering such as that on a hard shell PES. For such an instantaneous collision, the angular momentum transferred to the diatomic molecule must lie perpendicular to the direction of linear momentum transferred, or 'kinematic apse', $\mathbf{a_k} = \mathbf{k'} - \mathbf{k} / | \mathbf{k'} - \mathbf{k} |$. The alignment moments arising from these calculations have no dependence on the shape of the hard shell PES, depending entirely on the kinematics of the collisions. Calculations for individual collision energies were averaged over the two experimental collision energy distributions in the same manner as for the QS calculations.

C. Data Analysis

The experimentally-acquired images were analyzed in a procedure similar to that discussed in a previous publication, and only brief details will be given here except where the procedure differs from that described previously.[41] The image intensity I arising from molecules scattered with polar and azimuthal angles $\omega = (\theta,\phi)$ and detected using our (1 + 1') ionization scheme may be divided into a product of the DCS for the rotational state detected and an alignment-dependent detection probability I_{det}:[48]

$$I = \frac{d\sigma}{d\omega}(\theta) \times I_{\text{det}}\left(\phi, \mathbf{k}, A_{q+}^{\{2\}}(\theta), \chi\right) \tag{2}$$

$$I_{\text{det}}\left(\phi, \mathbf{k}, A_{q+}^{\{2\}}(\theta), \chi\right) = 1 + h^{\{2\}}\overline{g}^{\{2\}}\left(F_0^{\{2\}}A_0^{\{2\}}(\theta) + F_1^{\{2\}}A_{1+}^{\{2\}}(\theta) + F_2^{\{2\}}A_{2+}^{\{2\}}(\theta)\right) \tag{3}$$

where $\mathbf{k}$ is the initial relative velocity vector, χ is the angle between the scattering plane and the electric polarization vector of the probe laser, and $A_{q+}^{\{2\}}(\theta)$ are the non-zero second-rank scattering angle-dependent polarization moments. The $F_q^{\{2\}}$ pre-multipliers are geometrical terms which contain the dependence of the intensity on probe polarization, and have been given previously by Brouard *et al.*,[26] $h^{\{2\}}$ is the second-rank polarization sensitivity factor for one-photon probing,[48] and $\overline{g}^{\{2\}}$ is the appropriate time-averaged depolarization factor for Hund's case $b_{\beta J}$ coupling.[49]

Images for the H and V polarization geometries were generated using a Monte-Carlo simulation of the scattering. As described in previous publications,[40] the simulation sampled from the velocity distributions of the collider beams and generated a set of trajectories (typically 5 x 10^7) representing all possible scattering angles. The effect of collision with the two Ne isotopes was included in Monte-Carlo simulation through an additional selection step, in which the isotopic mass of the Ne was sampled from an appropriate distribution. Further details and example simulated images showing the effect of the isotopic Ne masses are presented in the Supplementary Material. The data necessary to simulate an image for any input DCS and set of alignment moments were then stored for later use in image simulation; this comprised the coordinates of the pixel at which the ion arrived, the polar scattering angle, and the $F_q^{\{2\}}$ terms for the H and V probe geometries.

Our previous work has demonstrated that a two-stage, iterative fitting procedure in which the DCS and alignment moments are treated as separable in their contributions to the images is an effective and efficient way to extract this information from the scattering images.[40] In the first stage of this process, an assumed set of alignment moments was treated as a fixed contribution to the images and the DCS was expanded as a linear combination of Legendre polynomials. For the

$\langle E_{col} \rangle$ = 523 cm^{-1} data, and the $\langle E_{col} \rangle$ = 1309 cm^{-1} data for N' = 14, a $P_\lambda(\cos\theta)$ basis was used. For the $\langle E_{col} \rangle$ = 1309 cm^{-1} data for final states N' = 3 - 13 a $P_\lambda(1 - \theta/90°)$ basis was used instead, since these functions were better able to represent the sharp features at small scattering angles evident in the data. The intensity at pixel (a,b) could then be expressed as:

$$I(a,b) = \sum_{\lambda=0}^{m_{DCS}-1} c_\lambda I_\lambda(a,b) \tag{4}$$

where each basis image $I_\lambda(a,b)$ corresponds to the λ^{th}-order Legendre polynomial in the expansion of the DCS, with coefficient c_λ. The pixel intensity for each basis image was then calculated as a sum over all trajectories contributing to that pixel:

$$I_\lambda(a,b) = \sum_{i=1}^{n_{ab}} P_\lambda I_{\text{det}} \tag{5}$$

The basis images were then convoluted with a 2D Gaussian chosen to model the detector response to individual ion strikes, and minor aberrations arising from the ion-optics. A downhill simplex χ^2 minimization algorithm was used to determine the best fit of the c_λ coefficients to the H and V images, with the DCS constrained to be positive by the imposition of a χ^2 penalty for values of the DCS less than zero.[50] The simplex algorithm underwent a series of restarts to ensure that the full parameter space was explored, with the output from the previous minimization used as one vertex of the simplex, and all others drawn from randomly selected, positive DCSs. The χ^2 tolerances for exit from each minimization and the cycle of restarts were each set based on a systematic exploration of the convergence properties for sample sets of data.

The resulting DCS was then used in the simulation of basis images which could be used to fit to the data to extract the polarization parameters. The pixel intensity may be expanded as a sum of basis images:

$$I(a,b) = I'(a,b) + \sum_{\lambda=0}^{m_{20}-1} c_\lambda^0 I_\lambda^0(a,b) + \sum_{\lambda=0}^{m_{21}-1} c_\lambda^1 I_\lambda^1(a,b) + \sum_{\lambda=0}^{m_{22}-1} c_\lambda^2 I_\lambda^2(a,b) \tag{6}$$

where each basis image depends on the DCS determined in the first fitting stage, and each $I_\lambda^q(a,b)$ image corresponds to the $P_\lambda(1 - \theta/90°)$ term in the expansion of the $A_{q+}^{\{2\}}(\theta)$ moment

$$I'(a,b) = \sum_{i=1}^{n_{ab}} \frac{d\sigma}{d\omega}(\theta_i) \tag{7}$$

$$I_\lambda^q(a,b) = \sum_{i=1}^{n_{ab}} \frac{d\sigma}{d\omega}(\theta_i)\, h^{\{2\}} \overline{g}^{\{2\}} F_q^{\{2\}} P_\lambda(1-\theta_i/90°) \tag{8}$$

The c_λ^q expansion coefficients were again determined through a χ^2 minimization algorithm, with restarts, as described above. Each alignment moment was constrained by the imposition of χ^2 penalties to lie within its physical limits. In addition, at the angles θ = 0° and 180° the constraints $A_0^{\{2\}}(\theta) = -1$ and $A_{1+}^{\{2\}}(\theta) = A_{2+}^{\{2\}}(\theta) = 0$ were applied. These reflect angular momentum conservation and symmetry constraints on the values of these moments for the cases where **k** and **k'** are parallel and anti-parallel, respectively. Further information on the implementation of these constraints in the fitting algorithm is available in the Supplementary Material.

The $A_{q+}^{\{2\}}(\theta)$ moments acquired in this step were then used in a repeat of the procedure to extract the DCS and all steps iterated until satisfactory agreement between the fitted values for the DCS and all $A_{q+}^{\{2\}}(\theta)$ moments was achieved on successive fitting cycles. The criterion for satisfactory agreement on successive cycles was that the values of the DCS and each polarization moment returned from successive fitting cycles was < 1% of their respective maximum absolute values, differences which are insignificant relative to the experimental error. For each product N', we report the mean of fits to eight individual pairs (H and V) of images acquired on different days, and quote errors as twice the standard error of the mean from these individual fits.

III. RESULTS

Figure 1 shows Newton diagrams for the low- and high-collision energy scattering to form N' = 8 superimposed onto the sum of images recorded in the V and H polarization geometries. Also shown is the 600 nm probe beam propagation direction $\mathbf{k_p}$. The average angle between **k** and $\mathbf{k_p}$ is 97° and 75° for the low- and high-energy collisions, respectively. As a consequence the sensitivity in either case to the $A_{1+}^{\{2\}}(\theta)$ moment is low,[26, 41] and while this moment was included in the analysis of the images, the associated uncertainties in their measured values are large, and consequently they are not presented or further discussed.

Figure 2 shows an example set of experimental images recorded in individual acquisitions for $\langle E_{col} \rangle$ = 523 cm^{-1}. Images in the V and H geometries are shown for all N' states probed, and are compared to the fits to these images. A corresponding set of images from scattering at $\langle E_{col} \rangle$ = 1309 cm^{-1} are shown together with fits in Fig. 3. The fitted images reproduce the experimental images very well, giving confidence in both the treatment of the scattering kinematics, and that a sufficient number of basis functions have been included in the parameterization of the DCS and alignment moments to capture the observed stereodynamical features. An area of localized noise can be seen at the bottom of the experimental images, outside of the scattering ring and coinciding with the lab frame velocity of the NO molecular beam. This signal arises from non-resonant ionization of unscattered NO(A) by the 532 nm laser pulse; the subtraction of this signal by recording background images of unscattered NO is imperfect, and this signal becomes more significant for higher-N' as the fluence of the ionization laser is increased to compensate for the low cross section for scattering into these states. For states in which this unwanted signal is appreciable, the affected pixels in the image were excluded from the fitting procedure. For the majority of N' states, the scattered ion signal and that arising from non-resonant ionization occur in clearly distinguishable regions of the images. The exception is the N' = 10 state for $\langle E_{col} \rangle$ = 523 cm^{-1}, where the forward-scattered portion of the Newton sphere overlapped with pixels excluded from the fit; for this reason, the DCS and alignment moments in this region could not be measured.

A number of features of the collision kinematics and dynamics are immediately apparent from inspection of the experimental images. The radii of the scattering images is required to decrease, of course, as N' increases and the fraction of the initial collision energy partitioned into center-of-mass translational kinetic energy decreases. A subtle asymmetry can be observed in those images for which there is substantial sideways scattering, e.g. $\langle E_{col} \rangle$ = 523 cm^{-1} N' = 7 and 8, in which the slow (left) side of the image is noticeably sharper than the fast (right) side. This arises from the kinematic blurring brought about by the spread of speeds in the molecular beams, which affects the two sides of the image differently. This is particularly clear in these experiments, as a result of the excellent signal-to-noise ratio and the equal sensitivity to fast and slow moving products enabled by the definite start time introduced by the pulsed laser preparation of the initial state. As is commonly observed in studies of rotational energy transfer, there is a general trend towards scattering at higher angles as N' increases. This trend is present but significantly less pronounced in the high energy scattering relative to the low energy scattering, and in none of the states for which the experimental signal-to-noise ratio was sufficient to obtain scattering data was a transition to primarily backward-scattered dynamics observed for the $\langle E_{col} \rangle$ = 1309 cm^{-1} collisions. The very clear difference between the vertical (V) and horizontal (H) images for both collision energies indicates a strong rotational angular momentum alignment.

The DCSs and scattering angle dependent alignment moments returned from the fits to the $\langle E_{col} \rangle$ = 523 cm^{-1} data are presented in Fig. 4. The fits are compared to the collision energy averaged QS calculations using both the PRRH and CF PESs, as well as the predictions of the KA model.[42, 43] Because no absolute cross section information is available from the experiments, for the purposes of this comparison, the experimental DCSs have been area normalized to the results of the QS calculations on the CF PES, excluding regions where the experimental and calculated DCSs clearly deviate, namely the 0-10° scattering angle range for all states. The majority of the experimentally measured behavior in the DCSs for $\langle E_{col} \rangle$ = 523 cm^{-1} scattering is very well reproduced by the QS calculations using both PESs. Both sets of calculations predict double maxima in the DCSs for N' = 5 and 7 with single maxima (although with some perceptible inflexions) for all other states, and the positions of these maxima are in very good agreement with experiment. The most significant deviations between experiment and theory occur for scattering angles below 10°, where the DCSs predicted by the scattering calculations are near-zero, while significant peaks are observed at 0° for N' = 3, 6, 7 and 8.

For scattering angles where the DCS is small, the uncertainties in the measured alignment moments become large, and hence we have restricted the reported values of the experimental alignment moments to angles at which the DCS is at least 10% of its maximum value, excluding the 0-10° forward scattered peak. The striking oscillatory behavior of the alignment moments, first reported in Ref. [39], is also observed here with a more extensive data set with substantially improved signal-to-noise, and a more rigorous analysis procedure. The QS calculations on the two PESs predict very similar alignment moments, and these predictions are in very good agreement in the angular ranges within which they were determined with the experimental moments, across the whole range of N' probed. Very large deviations from the KA predictions are observed for both experiment and QS calculations, particularly for scattering in the forward hemisphere. On close inspection, the strong oscillations in the alignment moments are correlated with the structure in the DCS, most clearly for N' = 5 and 7, where for $A_0^{\{2\}}(\theta)$ the sharp peaks to positive values occur at the same scattering angles ($\theta \approx 30°$ and 45° respectively) as the minima between the double maxima in the DCSs.

The DCSs and alignment moments returned by the fits to the $\langle E_{col} \rangle$ = 1309 cm^{-1} data are presented in Fig. 5. The data have again been area normalized to the CF QS results, excluding the 0-10° scattering angle range for all states, and the 90-180° scattering angle range for $N' \geq 11$. The forward scattered peaks in the experimentally measured DCSs are, again, not reproduced by the QS calculations, and while the general qualitative structure is similar at larger scattering angles for all but the highest rotational states probed, the level of agreement is poorer than for the low-energy scattering. The QS predictions differ most significantly from the experimental results for N' = 11 – 14, where an increasingly large backward scattered component to the DCS is predicted by both sets of calculations, for which there is no evidence in the experimental data. The

marked oscillations observed in the measured alignment moments at $\langle E_{col} \rangle$ = 523 cm^{-1} are not generally visible at this higher collision energy, and the strong forward scattering propensity limits the range of angles for which the moments can be reported. However, within the measureable range very good agreement is observed between the experimental measurements and the QS calculations. For $N' \geq 10$, where significant deviations between the QS and KA calculations are apparent, the behavior observed experimentally closely follows the QS results and is again poorly predicted by the KA model.

IV. DISCUSSION

The primary aim of this paper is to use the experimentally measured DCSs and rotational alignment parameters to give insight into the accuracy of the PRRH and CF PESs for the NO(A)-Ne system. Polar plots of these PESs are given in Fig. 6 together with the radial dependence of the Legendre moments of the two PESs, which we now briefly compare. Both PESs have very shallow absolute well depths, 3.75 cm^{-1} and 5.12 cm^{-1}, that occur at long ranges, R = 6.5 Å and 6.3 Å, for the PRRH and CF PESs respectively. On either PES, but not in a quantitatively identical fashion, the R-dependent gradient of the PESs varies significantly as a function of α at the energies accessed in these experiments. Approach of the Ne towards the 'N' end of the NO molecule is the most steeply repulsive, with a shallower gradient for approach to the 'O' end, and a much shallower gradient for side-on approach. This 'soft' repulsive wall is in marked contrast to the steep repulsive wall observed for the NO(X)-Ne PES.[43]

The *ab initio* energies were calculated on different angular grids, at 45° and 30° intervals for the PRRH and CF PESs, respectively. As a result, there are only 5 non-zero Legendre moments of the PRRH PES (l = 0 to 4), whereas there are 7 for the CF PES (l = 0 to 6). Substantial differences are seen in the l = 1 to 4 moments for the two PESs, reflecting differences in the anisotropies of the surfaces. Although the l = 1 moments have similar minimum negative values, this minimum lies at longer R for the CF PES. At shorter R, the l = 1 moment for the CF PES rises much more steeply. This indicates that the CF PES has a greater N-end to O-end anisotropy than the PRRH PES. Substantial differences are also observed for the l = 2 moment, where a considerably deeper minimum is observed for the CF PES compared to the PRRH PES (≈ -200 cm^{-1} vs. ≈ -100 cm^{-1}), reflecting a larger N-end/O-end versus side-on anisotropy for the CF PES. Similar trends are visible in the l = 3 and l = 4 moments of the two PESs. The l = 5 and 6 Legendre moments shown in Fig. 6(d) are negligible at the range of R accessed by the low-energy collisions, however, for the high-energy $\langle E_{col} \rangle$ = 1309 cm^{-1} collisions these moments make an appreciable contribution to the overall potential. Overall, the differences in the gross anisotropies in the PESs are summarized in Table I. This presents the radii, R, for the two average collision energy contours at 0° (Ne approaching N-end), 90° (Ne approaching side-on), and 180° (Ne approaching O-end) for the two PESs. The CF PES presents a larger difference in both

end-to-end and end-to-side R for both collision energies, and can thus be described as a more anisotropic PES than the PRRH PES.

We first examine the DCSs for scattering to angles greater than 10° where, as shown in the Section III, the QS calculations on both PESs show good agreement with the experimental measurements, although with substantially better agreement at $\langle E_{col} \rangle$ = 523 cm^{-1} than $\langle E_{col} \rangle$ = 1309 cm^{-1}. The occurrence of maxima in the DCS that shift to larger scattering angles with increasing N' is a characteristic manifestation of a rotational rainbow. Classically, the rainbow angle corresponds to the minimum angle at which sufficient translational momentum is converted to rotational angular momentum, with scattering to smaller angles being forbidden.[51-53] For a heteronuclear molecule such as NO, the differences in the PES for the two ends and location of the center-of-mass away from the bond axis centerpoint can result in two distinct rainbows, arising from the two ends of the molecule. As a consequence, the scattering angles at which the rainbow maxima appear are very sensitive to the form of the repulsive regions of the PES. The scattering angles corresponding to the rainbow maxima determined from the experimental DCSs and QS calculations are compared in Fig. 7. For the $\langle E_{col} \rangle$ = 523 cm^{-1}, the calculations on the CF PES provide significantly better agreement with experiment than those on the PRRH PES, with the latter consistently predicting rainbow angles larger than those measured experimentally. This indicates that the PRRH PES underestimates the degree of anisotropy in the NO(A)-Ne PES at this collision energy, and that the more anisotropic CF PES better represents the real NO(A)-Ne interaction. The level of agreement with experiment for both PESs is worse at $\langle E_{col} \rangle$ = 1309 cm^{-1}, although for the majority of product N' the CF PES again provides better predictions. This suggests that both the CF and PRRH PESs are increasingly inaccurate at higher collision energies, consistent with the lower number of *ab initio* points calculated at these higher energies.[42, 43] While overall performing better than the PRRH PES in predicting the first rainbow maximum, the CF PES did not predict the location of the secondary maxima for the N' = 5 and 7 states at $\langle E_{col} \rangle$ = 523 cm^{-1} as accurately, and also predicted substantially larger relative cross sections for the secondary maxima. As discussed above, multiple rotational rainbow peaks arise from scattering from different ends of the molecule, and the poorer prediction of the position and intensity of the second rainbow peak is consistent with larger errors in the odd Legendre moments of the CF PES than in the even moments.[53]

The most significant disagreement in the DCS between experiment and theory is in the forward-scattered (θ < 10°) region, where large peaks are observed experimentally for a wide range of N', but are not predicted by theory on either PES. We have taken particular care to exclude experimental artefact as the cause of this disagreement. As discussed in the experimental and results sections, we have ensured that signals associated with non-resonant ionization by the 532 nm laser pulse have been subtracted from the fitted images where possible, and we have also excluded residual noise in the affected

regions from the fitting procedure. We are confident that such signals are not the origin of the reported 0-10° forward scattering. We also considered whether the forward scattered peaks were associated with fitting algorithm artefacts. A relatively small number of pixels determine the scattering amplitude in the extreme forward and backward directions, compared to sideways angles. In addition, the kinematic blurring associated with the spread of speeds in the molecular beams results in the lowest angular resolution for 0° and 180°. These effects can be seen in the relatively large error bars reported for these extreme scattering angles. Nevertheless, the large forward scattered peaks and disagreement with theory are not a fitting artefact. This is demonstrated in Figure 8, which compares experimental images (sum of the V+H geometries, averaged across all 8 independent measurements) for $N' = 3$ and 7 with simulations based on the results of the QS calculations on the CF PES, for both $\langle E_{col} \rangle$. The simulations do not agree well with the experimental data in the extreme forward direction, with the experiment having noticeably greater intensity in this region, consistent with the scattering peak recovered by the fitting algorithm. The preliminary experiments on NO(A) + Ne scattering, performed in a different apparatus at Sandia National Laboratory and reported in Ref. [39], also showed strong scattering into the 0-10° range, although for a smaller range of product N' and with poorer signal-to-noise. We therefore believe that this is a genuine feature of the scattering dynamics.

This forward-scattered component is characteristic of a *L*-type rainbow, which results from an attractive well on the PES, and for this to result in rotational excitation the attractive well must be anisotropic.[54] As previously discussed, neither the PRRH nor the CF PES has an appreciable attractive well, and the very shallow long range wells that are present on those surfaces are essentially isotropic, represented as the minima in the $l = 0$ Legendre components of the PESs in Fig. 6(b) and 6(d). This is consistent with the absence of any *L*-type rainbow scattering in the QS calculations. We therefore infer that the *ab initio* calculations have failed to capture a (presumably) shallow but still significant anisotropic well at moderate *R* that results in the experimentally observed *L*-type rainbow scattering. We have previously provided strong evidence that a similar, but more prominent, feature in the DCSs for scattering of NO(A) with Ar arises from the presence of an attractive well for a collinear geometry with the Ar atom at the N-end of the molecule, consistent with the *ab initio* PES for the NO(A)-Ar system.[40, 43, 55] We note that for NO(A) + Ar scattering, both in the experimental and QS results, these *L*-type rainbows were observed to peak at 0°, consistent with the experimental measurements reported here for NO(A) + Ne. Similar, but deeper, attractive wells at the N-end of NO are seen in the *ab initio* NO(A)-Kr and NO(A)-Xe PESs, which also extend to an increasingly wider angular range around the co-linear Rg-N-O geometry.[55] If there is a shallow (but sufficiently deep to support at least one bound state) well on the NO(A)-Ne PES, it should, in principle, be possible to probe it by spectroscopy of the NO(X)-Ne van der Waals complex. Ayles *et al.* measured (1 + 1) (A-X) REMPI spectra of the complexes of NO(X) with Ne, Ar, Kr and Xe.[56] While transitions from NO(X)-Rg complexes to bound rovibrational levels of NO(A)-Rg complexes were observed for Rg = Ar, Kr and Xe, no signals were observed from NO(X)-Ne complexes. Although this was noted to be

consistent with the absence of a well on the PRRH PES, it could also be explained as the result of very small Franck-Condon factors for the NO-Rg(A-X) transition. The equilibrium geometry for the NO(X)-Ne complex is T-shaped with R = 3.3 Å, and overlap of the bound vibrational wavefunctions of this complex with a relatively shallow NO(A)-Ne well that is tightly focused around the collinear Ne-N-O geometry will be very poor. For comparison, the measured dissociation energy for NO(A)-Ar is $D_0 \approx 50$ cm^{-1}, and we anticipate that the NO(A)-Ne well will be shallower than this.[57] This is an example of how bimolecular scattering experiments can provide complementary insight into the NO(A)-Ne PES, since the range of geometries explored is not constrained by the vibrational structure of the ground state NO(X)-Ne complex, as it is in spectroscopic or photodissociation experiments.[58] We note that *ab initio* calculations of the NO(A)-Ar PES have also consistently underestimated the experimentally-measured depth of the attractive well on this surface; the RCCSD(T) PES of Kłos *et al.*[55] required scaling by a factor of 1.23 to bring the well-depth in line with that measured spectroscopically, and more recent CASSCF-MRCI and RCCSD(T) calculations have not improved on this discrepancy.[43, 59] Further theoretical work will be required to address what appears to be a consistent underestimation of the strength of the attractive interactions in these systems.

A further feature of the stereodynamics measured experimentally and predicted in the QS calculations is behavior that alternates with final N'. In particular, the DCSs for $\langle E_{col} \rangle$ = 523 cm^{-1} scattering exhibit an alternation in the number of rotational rainbow peaks over the range N' = 5 - 8, with double maxima for odd-N' and single maxima for even N'. A clear alternation is also apparent in the high collision energy scattering, with the DCS significantly more sideways-scattered for the even states than for the odd states, which is evident from a simple inspection of the raw images in Fig. 3. Scattering from N = 0 to even- and odd-N' has the effect of conserving and changing the parity of the NO(A) rotational wavefunction, respectively, and there is extensive literature on the impact on the DCS of parity conserving/changing collisions in RET of $^2\Sigma$-systems.[3, 4, 44, 60-62] As has been discussed widely , even/odd alternations in the integral cross-sections can be related to the influence of the even and odd Legendre moments of the PES, as within the Born approximation only the even moments couple initial and final states of the same parity, while only odd moments couple states of different parity.[44, 60, 61] Transitions in which ΔN is large are likely to be poorly described by the Born approximation, but can be considered in a framework of virtual transitions through intermediate N'.[25, 63-65] While ΔN = odd overall transitions can incorporate ΔN = even virtual transitions, they must involve an odd number of ΔN = odd virtual transitions. Therefore parity-changing collisions must sample the odd parts of the PES. In contrast, ΔN = even overall transitions can be constructed from pathways that include odd virtual transitions, and from pathways that *only* include even virtual transitions. Thus, overall ΔN = even and ΔN = odd transitions sample different effective PESs, with a bias towards even- and odd-l Legendre moments respectively. Although, as discussed, there is generally very good agreement between experiment and theory for the DCSs excluding the L-type

rainbow peak, for the $\langle E_{col} \rangle$ = 1309 cm^{-1} results, Fig. 5 and Fig. 7(b) show a clear even/odd pattern of disagreement. Comparing experiment and theory on the CF PES, for the N' = 9 - 14 range of product states there is a clear pattern of relatively good agreement in the location of the rainbow scattering peak for odd-N', and systematic overstatement of the rainbow peak scattering angle for even-N'. Within the framework outlined here, this implies that the even moments of the PES sampled at this high collision energy are less accurate than the odd moments.

Turning to the alignment moments, we first again note the generally very good agreement between the experimental measurements and the QS results on both the PRRH and CF PESs. Precise measurement of the alignment moments, as it relies on differences between the V and H geometry images, is necessarily harder than measurement of the DCS. As a result, the alignment measurements are generally not able to distinguish one PES over another. In the few cases where the calculated alignment moments are very different, e.g. around 90° for N' = 3 at $\langle E_{col} \rangle$ = 523 cm^{-1} or 45-90° for N' = 5 at $\langle E_{col} \rangle$ = 1309 cm^{-1} it is often the case that the experimentally observed scattering amplitude was too small for effective determination of the alignment moments.

However, a clear conclusion from the experimental measurements is that the KA model does not provide a good description of the dynamics, and that the QS calculations are much closer to the experimentally measured values. We have previously measured alignment moments that depart substantially from the KA behavior for NO(A) + He/D_2 scattering, and have shown that images recorded for NO(A) + Ar and NO(A) + Ne scattering are consistent with the QS predictions of alignment moments exhibiting significant oscillatory structure that cannot be reproduced by the KA model.[39, 40] In those studies, we noted that the PESs for these three NO(A)-Rg collision systems have relatively shallow gradients along R, and it is therefore perhaps unsurprising that the KA calculations, relying as they do on a hard-shell model of the PES, should be unsuccessful in reproducing the experimental measurements. Nevertheless, a satisfactory explanation for the link between the features of these PESs and the form of the departures from the KA model has yet to be provided. As noted in Section III, the deviations from KA-behavior are correlated with the structure in the DCS, which is particularly clear for N' = 5 and 7 at $\langle E_{col} \rangle$ = 523 cm^{-1}, where a large deviation is observed at scattering angles corresponding to the rainbow maxima, with a recovery to close to the KA prediction at the intervening minimum. It is entirely possible that classical modelling on the accurate, non-rigid, PES would reproduce multiple rainbow angle scattering, corresponding to scattering in this case from the two ends of the NO molecule. It is certainly also possible that such scattering would also result in non-KA alignment moments. It seems unlikely to us, *a priori*, that a purely classical scattering calculation would reproduce the rapid oscillation in the alignment moments. In classical scattering, the minimum between the two rainbow maxima has no special significance, and is merely a consequence of the separation of the rainbow scattering peaks from either end of the molecule and their

relative widths. There seems little reason for a rapid change in the angular momentum polarization arising from classical scattering into this narrow range of angles. We therefore believe that it is probable that a QM interference effect is responsible for this striking behavior.

V. CONCLUSION

We have studied the stereodynamics of NO(A) + Ne scattering at mean collision energies of 523 cm^{-1} and 1309 cm^{-1}, and have reported experimental measurements of the rotational state-to-state DCSs and angle-dependent rotational angular momentum alignment moments for scattering of NO($A^2\Sigma^+$; v = 0; $N = 0$, $j = ½$) into a range of final N'. Comparison with QS calculations has provided a stringent test of the two *ab initio* PESs available for NO(A)-Ne, enabling us to compare the accuracy of the PESs, and to suggest areas in which they may be improved. The observation of a forward-scattered component to the DCSs for a range of final N' that is not reproduced in the calculations, strongly suggests that both PESs underestimate the degree of attractive interactions for the NO(A)-Ne system. While both sets of calculations qualitatively reproduce the rotational rainbow structures observed at larger scattering angles, a quantitative comparison suggests that the more recent PES of Cybulski *et al.* provides a more accurate description of the angular variation of the repulsive region of the true PES. The measured alignment moments closely follow the QS calculations, and demonstrate oscillations as a function of scattering angle that cannot be reproduced by a hard shell model of the scattering. The ability to distinguish between the quality of two sets of high-level *ab initio* electronic structure calculations demonstrates the exquisite sensitivity of direct measurements of RET stereodynamics to the topography of the underlying PES.

SUPPLEMENTARY MATERIAL

See the Supplementary Material for details of the determination of the collider speed distributions, of the effect of different isotopic masses of the Ne collider on image simulation, and of the implementation of constraints on the fitting of the alignment moments.

ACKNOWLEDGEMENTS

This work was supported by the U.K. EPSRC *via* grant EP/J017973/01. T.F.M.L. acknowledges Heriot-Watt University for a James Watt PhD scholarship. We also acknowledge the assistance of P. J. Dagdigian, J. Kłos and M. H. Alexander in performing the quantum scattering calculations. Raw data on which this publication is based can be accessed via the Heriot-Watt University Data Repository.

REFERENCES

1. R. P. Wayne, *Chemistry of Atmospheres,* Third ed. (Oxford University Press, Oxford, 2000).
2. E. Roueff and F. Lique, Chem Rev **113**, 8906 (2013).
3. A. Schiffman and D. W. Chandler, Int Rev Phys Chem **14**, 371 (1995).
4. P. J. Dagdigian, in *The Chemical Dynamics and Kinetics of Small Radicals*, Advanced Series in Physical Chemistry, edited by K. Liu and A. J. Wagner (World Scientific, Singapore, 1995), p. 315.
5. J. J. Gilijamse, S. Hoekstra, S. Y. T. van de Meerakker, G. C. Groenenboom, and G. Meijer, Science **313**, 1617 (2006).
6. M. Kirste, L. Scharfenberg, J. Kłos, F. Lique, M. H. Alexander, G. Meijer, and S. Y. T. van de Meerakker, Phys Rev A **82**, 042717 (2010).
7. L. Scharfenberg, K. B. Gubbels, M. Kirste, G. C. Groenenboom, A. van der Avoird, G. Meijer, and S. Y. T. van de Meerakker, Eur Phys J D **65**, 189 (2011).
8. L. Scharfenberg, J. Kłos, P. J. Dagdigian, M. H. Alexander, G. Meijer, and S. Y. T. van de Meerakker, Phys Chem Chem Phys **12**, 10660 (2010).
9. H. C. Schewe, Q. L. Ma, N. Vanhaecke, X. A. Wang, J. Kłos, M. H. Alexander, S. Y. T. van de Meerakker, G. Meijer, A. van der Avoird, and P. J. Dagdigian, J Chem Phys **142**, 204310 (2015).
10. M. L. Costen, S. Marinakis, and K. G. McKendrick, Chem Soc Rev **37**, 732 (2008).
11. G. Paterson, M. L. Costen, and K. G. McKendrick, Int Rev Phys Chem **31**, 69 (2012).
12. H. Chadwick, M. Brouard, T. Perkins, and F. J. Aoiz, Int Rev Phys Chem **33**, 79 (2014).
13. S. J. McGurk, K. G. McKendrick, M. L. Costen, M. H. Alexander, and P. J. Dagdigian, J Chem Phys **139**, 124304 (2013).
14. G. Sarma, S. Marinakis, J. J. ter Meulen, D. H. Parker, and K. G. McKendrick, Nat Chem **4**, 985 (2012).
15. L. Song, G. C. Groenenboom, A. van der Avoird, C. K. Bishwakarma, G. Sarma, D. H. Parker, and A. G. Suits, J Phys Chem A **119**, 12526 (2015).
16. C. K. Bishwakarma, G. van Oevelen, R. Scheidsbach, D. H. Parker, Y. Kalugina, and F. Lique, J Phys Chem A **120**, 868 (2016).
17. K. T. Lorenz, M. S. Westley, and D. W. Chandler, Phys Chem Chem Phys **2**, 481 (2000).
18. O. Tkac, A. G. Sage, S. J. Greaves, A. J. Orr-Ewing, P. J. Dagdigian, Q. L. Ma, and M. H. Alexander, Chem Sci **4**, 4199 (2013).
19. C. H. Yang, G. Sarma, J. J. ter Meulen, D. H. Parker, U. Buck, and L. Wiesenfeld, J Phys Chem A **114**, 9886 (2010).
20. O. Tkac, A. K. Saha, J. Loreau, Q. L. Ma, P. J. Dagdigian, D. H. Parker, A. van der Avoird, and A. J. Orr-Ewing, Mol Phys **113**, 3925 (2015).
21. H. Kohguchi, T. Suzuki, and M. H. Alexander, Science **294**, 832 (2001).
22. K. T. Lorenz, D. W. Chandler, J. W. Barr, W. W. Chen, G. L. Barnes, and J. I. Cline, Science **293**, 2063 (2001).
23. A. Gijsbertsen, H. Linnartz, G. Rus, A. E. Wiskerke, S. Stolte, D. W. Chandler, and J. Kłos, J Chem Phys **123**, 224305 (2005).
24. E. A. Wade, K. T. Lorenz, D. W. Chandler, J. W. Barr, G. L. Barnes, and J. I. Cline, Chem Phys **301**, 261 (2004).
25. C. J. Eyles, M. Brouard, C. H. Yang, J. Kłos, F. J. Aoiz, A. Gijsbertsen, A. E. Wiskerke, and S. Stolte, Nat Chem **3**, 597 (2011).
26. M. Brouard, H. Chadwick, C. J. Eyles, B. Hornung, B. Nichols, F. J. Aoiz, P. G. Jambrina, and S. Stolte, J Chem Phys **138**, 104310 (2013).
27. M. Brouard, H. Chadwick, C. J. Eyles, B. Hornung, B. Nichols, J. M. Scott, F. J. Aoiz, J. Kłos, S. Stolte, and X. Zhang, Mol Phys **111**, 1759 (2013).
28. M. Brouard, H. Chadwick, S. D. S. Gordon, B. Hornung, B. Nichols, J. Kłos, F. J. Aoiz, and S. Stolte, J Chem Phys **141**, 164306 (2014).
29. B. Nichols, H. Chadwick, S. D. S. Gordon, C. J. Eyles, B. Hornung, M. Brouard, M. H. Alexander, F. J. Aoiz, A. Gijsbertsen, and S. Stolte, Chem Sci **6**, 2202 (2015).
30. M. Brouard, H. Chadwick, S. D. S. Gordon, B. Hornung, B. Nichols, F. J. Aoiz, and S. Stolte, J Phys Chem A **119**, 12404 (2015).
31. M. Brouard, H. Chadwick, S. D. S. Gordon, B. Hornung, B. Nichols, F. J. Aoiz, and S. Stolte, J Chem Phys **144**, 224301 (2016).
32. H. Chadwick, B. Nichols, S. D. S. Gordon, B. Hornung, E. Squires, M. Brouard, J. Kłos, M. H. Alexander, F. J. Aoiz, and S. Stolte, J Phys Chem Lett **5**, 3296 (2014).
33. S. N. Vogels, J. Onvlee, A. von Zastrow, G. C. Groenenboom, A. van der Avoird, and S. Y. T. van de Meerakker, Phys Rev Lett **113**, 263202 (2014).

34. A. von Zastrow, J. Onvlee, S. N. Vogels, G. C. Groenenboom, A. van der Avoird, and S. Y. T. van de Meerakker, Nat Chem **6**, 216 (2014).
35. S. N. Vogels, J. Onvlee, S. Chefdeville, A. van der Avoird, G. C. Groenenboom, and S. Y. T. van de Meerakker, Science **350**, 787 (2015).
36. J. Onvlee, S. N. Vogels, A. D. van der Avoird, G. C. Groenenboom, and S. Y. T. van de Meerakker, New J Phys **17**, 055019 (2015).
37. J. J. Kay, G. Paterson, M. L. Costen, K. E. Strecker, K. G. McKendrick, and D. W. Chandler, J Chem Phys **134**, 091101 (2011).
38. J. J. Kay, J. D. Steill, J. Kłos, G. Paterson, M. L. Costen, K. E. Strecker, K. G. McKendrick, M. H. Alexander, and D. W. Chandler, Mol Phys **110**, 1693 (2012).
39. J. D. Steill, J. J. Kay, G. Paterson, T. R. Sharples, J. Kłos, M. L. Costen, K. E. Strecker, K. G. McKendrick, M. H. Alexander, and D. W. Chandler, J Phys Chem A **117**, 8163 (2013).
40. T. R. Sharples, T. F. M. Luxford, D. Townsend, K. G. McKendrick, and M. L. Costen, J Chem Phys **143**, 204301 (2015).
41. T. F. M. Luxford, T. R. Sharples, D. Townsend, K. G. McKendrick, and M. L. Costen, J Chem Phys **145**, 084312 (2016).
42. P. Pajon-Suarez, G. Rojas-Lorenzo, J. Rubayo-Soneira, and R. Hernandez-Lamoneda, Chem Phys Lett **421**, 389 (2006).
43. H. Cybulski and B. Fernandez, J Phys Chem A **116**, 7319 (2012).
44. G. C. Corey, M. H. Alexander, and J. Schaefer, J Chem Phys **85**, 2726 (1986).
45. HIBRIDON is a package of programs for the time-independent quantum treatment of inelastic collisions and photodissociation written by M. H. Alexander, D. E. Manolopoulos, H.-J. Werner, B. Follmeg, and P. J. Dagdigian, with contributions by D. Lemoine, P. Vohralik, G. Corey, B. Johnson, T. Orlikowski, A. Berning, A. Degli-Esposti, C. Rist, B. Pouilly, J. Kłos, Q. Ma, G. van der Sanden, M. Yang, F. de Weerd, S. Gregurick, and F. Lique. More information and/or a copy of the code can be obtained from the website http://www2.chem.umd.edu/groups/alexander/hibridon/hib43.
46. R. C. Woods and T. A. Dixon, J Chem Phys **64**, 5319 (1976).
47. V. Khare, D. J. Kouri, and D. K. Hoffman, J Chem Phys **74**, 2275 (1981).
48. U. Fano and J. H. Macek, Rev Mod Phys **45**, 553 (1973).
49. R. Altkorn, R. N. Zare, and C. H. Greene, Mol Phys **55**, 1 (1985).
50. W. H. Press, S. A. Teukolsky, W. T. Vetterling, and B. P. Flannery, *Numerical Recipes in Fortran 90* (Cambridge University Press, Cambridge, 1996).
51. S. Bosanac, Phys Rev A **22**, 2617 (1980).
52. H. J. Korsch and R. Schinke, J Chem Phys **73**, 1222 (1980).
53. S. Bosanac and U. Buck, Chem Phys Lett **81**, 315 (1981).
54. R. D. Levine and R. B. Bernstein, *Molecular Reaction Dynamics and Chemical Reactivity* (Oxford University Press, New York, 1987).
55. J. Kłos, M. H. Alexander, R. Hernandez-Lamoneda, and T. G. Wright, J Chem Phys **129**, 244303 (2008).
56. V. L. Ayles, R. J. Plowright, M. J. Watkins, T. G. Wright, J. Kłos, M. H. Alexander, P. Pajon-Suarez, J. Rubayo-Soneira, and R. Hernandez-Lamoneda, Chem Phys Lett **441**, 181 (2007).
57. H. L. Holmes-Ross and W. D. Lawrance, J Chem Phys **135**, 014302 (2011).
58. H. L. Holmes-Ross, R. J. Valenti, H. G. Yu, G. E. Hall, and W. D. Lawrance, J Chem Phys **144**, 044309 (2016).
59. J. C. Castro-Palacio, K. Ishii, J. Rubayo-Soneira, and K. Yamashita, J Chem Phys **131**, 044506 (2009).
60. M. H. Alexander, J. E. Smedley, and G. C. Corey, J Chem Phys **84**, 3049 (1986).
61. M. H. Alexander, J Chem Phys **76**, 3637 (1982).
62. P. J. Dagdigian, Annu Rev Phys Chem **48**, 95 (1997).
63. M. H. Alexander, J Chem Phys **64**, 4498 (1976).
64. J. Kłos, F. J. Aoiz, J. E. Verdasco, M. Brouard, S. Marinakis, and S. Stolte, J Chem Phys **127**, 031102 (2007).
65. C. J. Eyles, M. Brouard, H. Chadwick, F. J. Aoiz, J. Kłos, A. Gijsbertsen, X. Zhang, and S. Stolte, Phys Chem Chem Phys **14**, 5420 (2012).

FIG. 1. Newton diagrams for the collision of NO(A) with Ne at (a) $\langle E_{col} \rangle$ = 523 cm^{-1} and (b) $\langle E_{col} \rangle$ = 1309 cm^{-1} overlaid on V + H experimental images for product state N' = 8. Arrows indicate the velocity vectors of the colliders: $\mathbf{v_{NO}}$, $\mathbf{v_{Ne}}$, the center of mass velocity: $\mathbf{v_{CoM}}$, and the relative velocity vector, $\mathbf{k}$. The ring represents the mean velocity of NO scattered into the plane of the detector. $\mathbf{k_p}$ indicates the propagation direction of the probe laser beam.
(*Single column*)

FIG. 2. Example single acquisition experimental images for the collision of NO(A, v = 0, N = 0, j = 0.5) with Ne at $\langle E_{col} \rangle$ = 523 cm^{-1}, for product states N' = 3 and 5-10 and for both H and V probe laser polarizations, together with images obtained from the fitting routine.
(*Double column*)

FIG. 3. Single acquisition experimental images for the inelastic collision of NO(A, v = 0, N = 0, j = 0.5) with Ne at $\langle E_{col} \rangle$ = 1309 cm^{-1}, for product states N' = 3 and 5-14 and for both H and V probe laser polarizations, together with images obtained from the fitting routine.
(*Double column*)

FIG. 4. Differential cross sections and rotational angular momentum polarization moments, $A_{q+}^{\{2\}}(\theta)$, for the inelastic collisions of NO(A) with Ne at $\langle E_{col} \rangle$ = 523 cm^{-1} for product states N' = 3, 5-10. Black line: results of fitting to experimental images (error bars represent 95% confidence limits), red line: results of energy averaged QS calculations run on the CF PES, blue line: results of energy averaged QS calculations run on the PRRH PES, dashed green (for $A_{q+}^{\{2\}}(\theta)$ only): results of energy averaged kinematic apse calculations.
(*Double column*)

FIG. 5. Differential cross sections and rotational angular momentum polarization moments, $A_{q+}^{\{2\}}(\theta)$, for the inelastic collisions of NO(A) with Ne at $\langle E_{col} \rangle$ = 1309 cm^{-1} for product states N' = 3, 5-14. Black line: results of fitting to experimental images (error bars represent 95% confidence limits), red line: results of energy averaged QS calculations run on the CF PES, blue line: results of energy averaged QS calculations run on the PRRH PES, dashed green (for $A_{q+}^{\{2\}}(\theta)$ only): results of energy averaged kinematic apse calculations.
(*Double column*)

FIG. 6. (a) and (c) Polar contour plots of the PRRH and CF PES, respectively. Solid black contour, 0 cm^{-1}. Dashed red contours, 0-100 cm^{-1} in 10 cm^{-1} intervals. Solid red contours, 100-1500 cm^{-1} in 100 cm^{-1} intervals. Solid blue contours, 523 cm^{-1} and 1309 cm^{-1}, representing the two average collision energies used in the experiments. (b) and (d) Radial dependence of the Legendre moments of the PRRH and CF PES, respectively, with insets on an expanding vertical scale to show the shallow, long-range isotropic wells present on both surfaces.
(*Double column*)

FIG. 7. Plots showing the rotational rainbow angle of the DCSs, as a function of N' at (a) $\langle E_{col} \rangle$ = 523 cm^{-1}, (b) $\langle E_{col} \rangle$ = 1309 cm^{-1}. Black squares, experimental results; red circles, QS calculation results from the CF PES; blue triangles, QS calculation results from the PRRH PES. Points enclosed by boxes are the maxima for the second rainbow feature apparent in the DCS for states where these features are clearly distinguishable. Experimental points are the mean from multiple independent measurements of the DCS, error bars represent 2 standard errors of the mean.
(*Single column*)

FIG. 8. Comparison of simulated V + H images, using the results of QS calculations on the CF PES, to experimental V + H images for N' = 3 and 7, at $\langle E_{col} \rangle$ = 523 cm^{-1} and $\langle E_{col} \rangle$ = 1309 cm^{-1}.
(*Single column*)

Table I. Radii, R, of the 523 cm^{-1} and 1309 cm^{-1} average experimental collision energy contours of the CF and PRRH PESs at 0°, 90° and 180° Ne-N-O angles, where 0° represents the linear Ne-N-O geometry.

		523 cm^{-1}	**1309 cm^{-1}**
PES	Angle	R / Å	R / Å
PRRH	0°	3.07	2.88
	90°	3.12	2.34
	180°	2.99	2.72
CF	0°	3.03	2.84
	90°	3.11	2.12
	180°	2.70	2.41

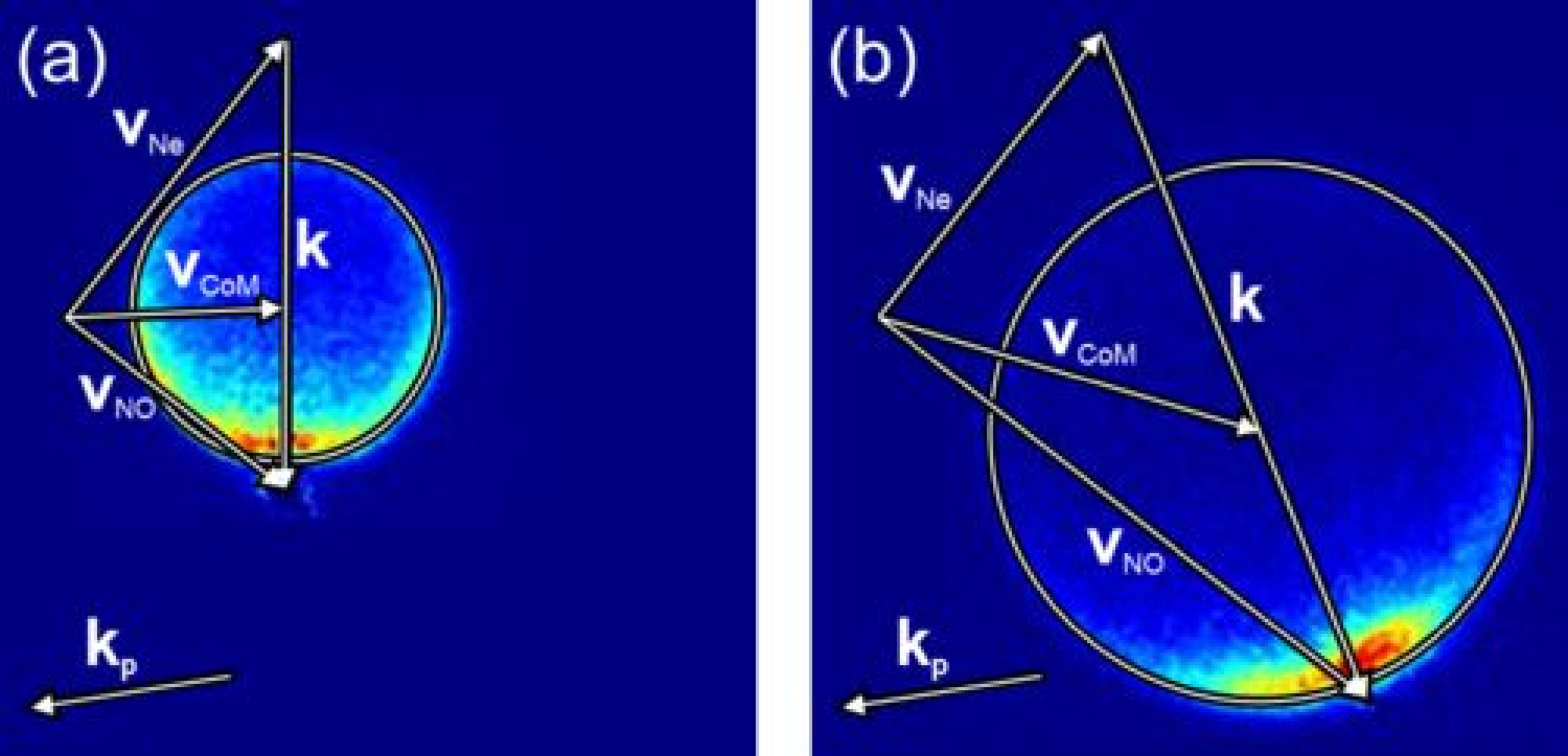
(a)
v_{Ne}
v_{CoM}
k
v_{NO}
k_p
(b)
v_{Ne}
k
v_{CoM}
v_{NO}
k_p

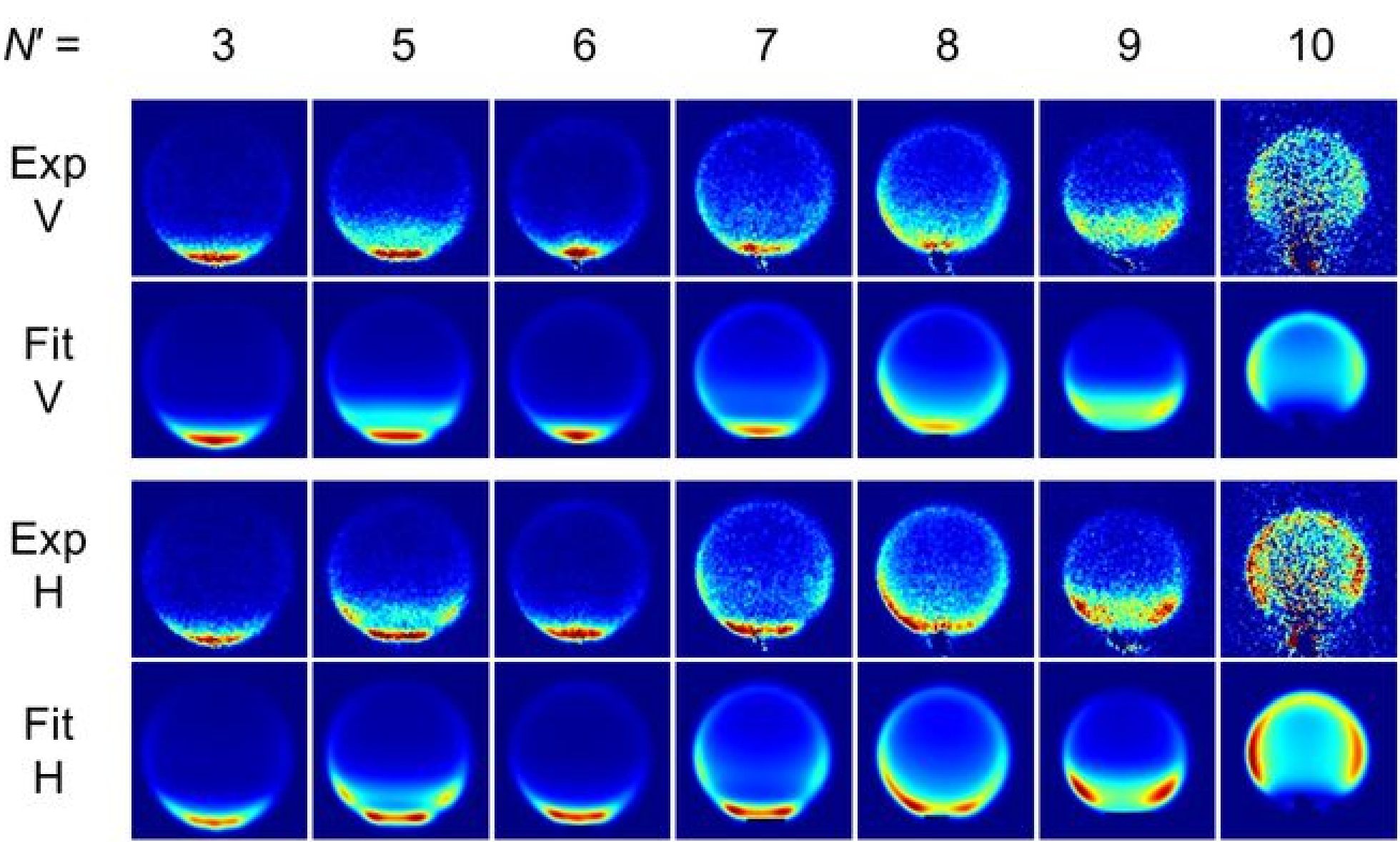
N′ =
3
5
6
7
8
9
10
Exp V
Fit V
Exp H
Fit H

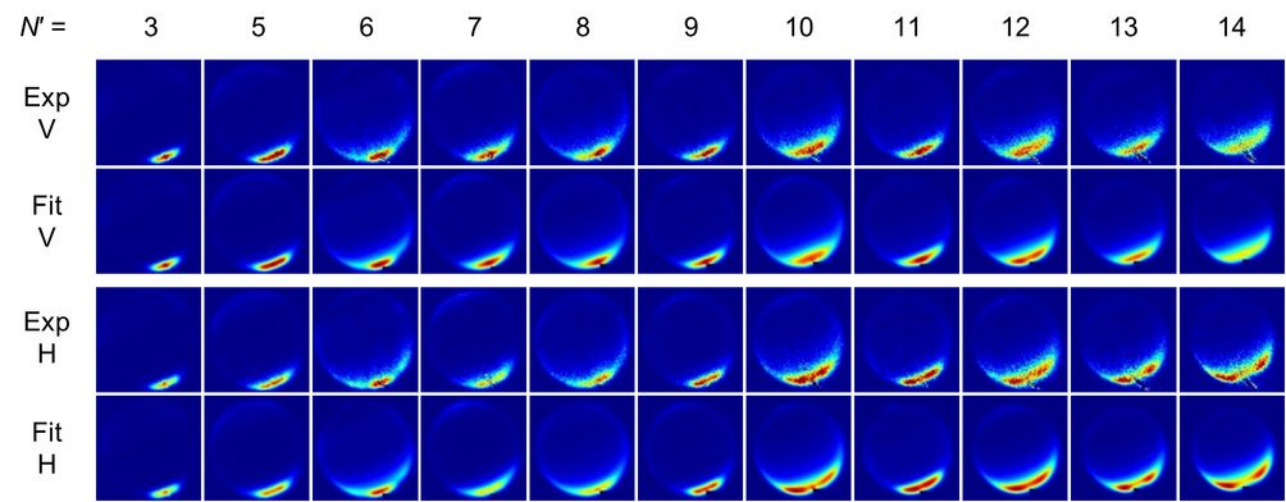
N′ =
3
5
6
7
8
9
10
11
12
13
14
Exp V
Fit V
Exp H
Fit H

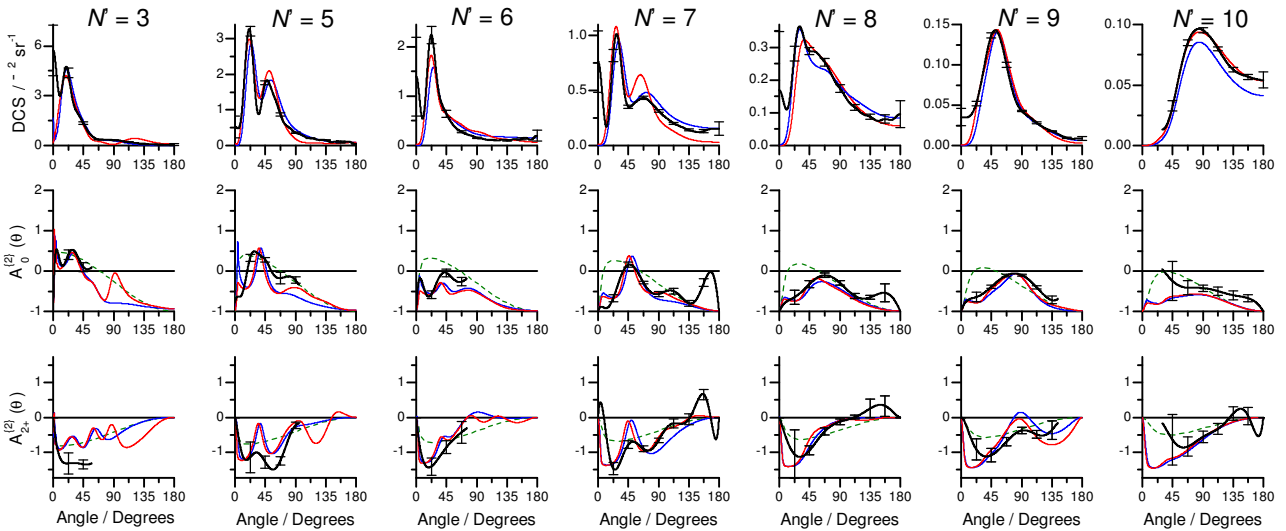
N' = 3
N' = 5
N' = 6
N' = 7
N' = 8
N' = 9
N' = 10
DCS / - 2 sr-1
A(2)0 (θ)
A(2)2- (θ)
0 45 90 135 180
Angle / Degrees

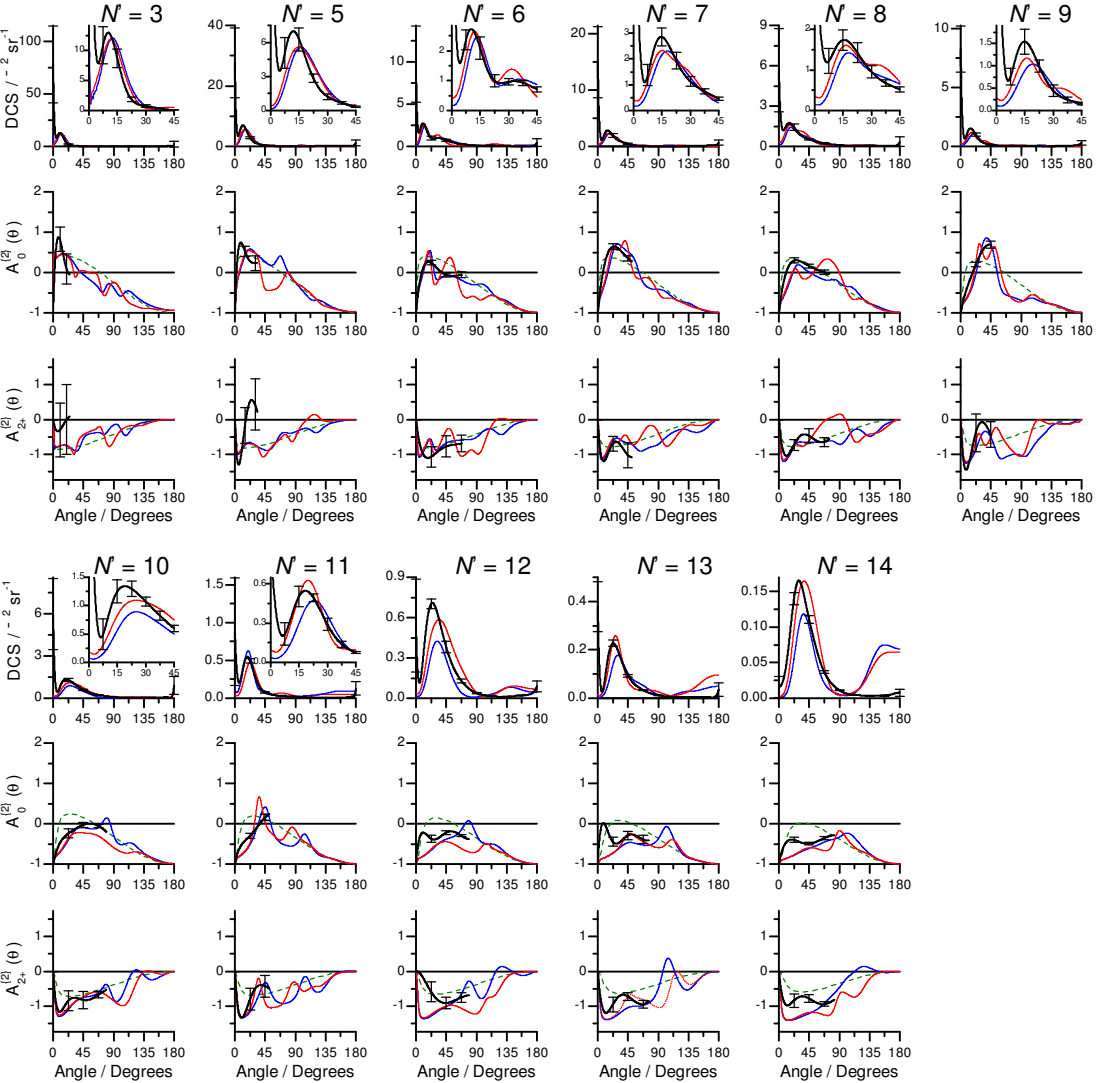
N' = 3
N' = 5
N' = 6
N' = 7
N' = 8
N' = 9
N' = 10
N' = 11
N' = 12
N' = 13
N' = 14
DCS / - 2 sr-1
A0(2) (θ)
A2+(2) (θ)
Angle / Degrees

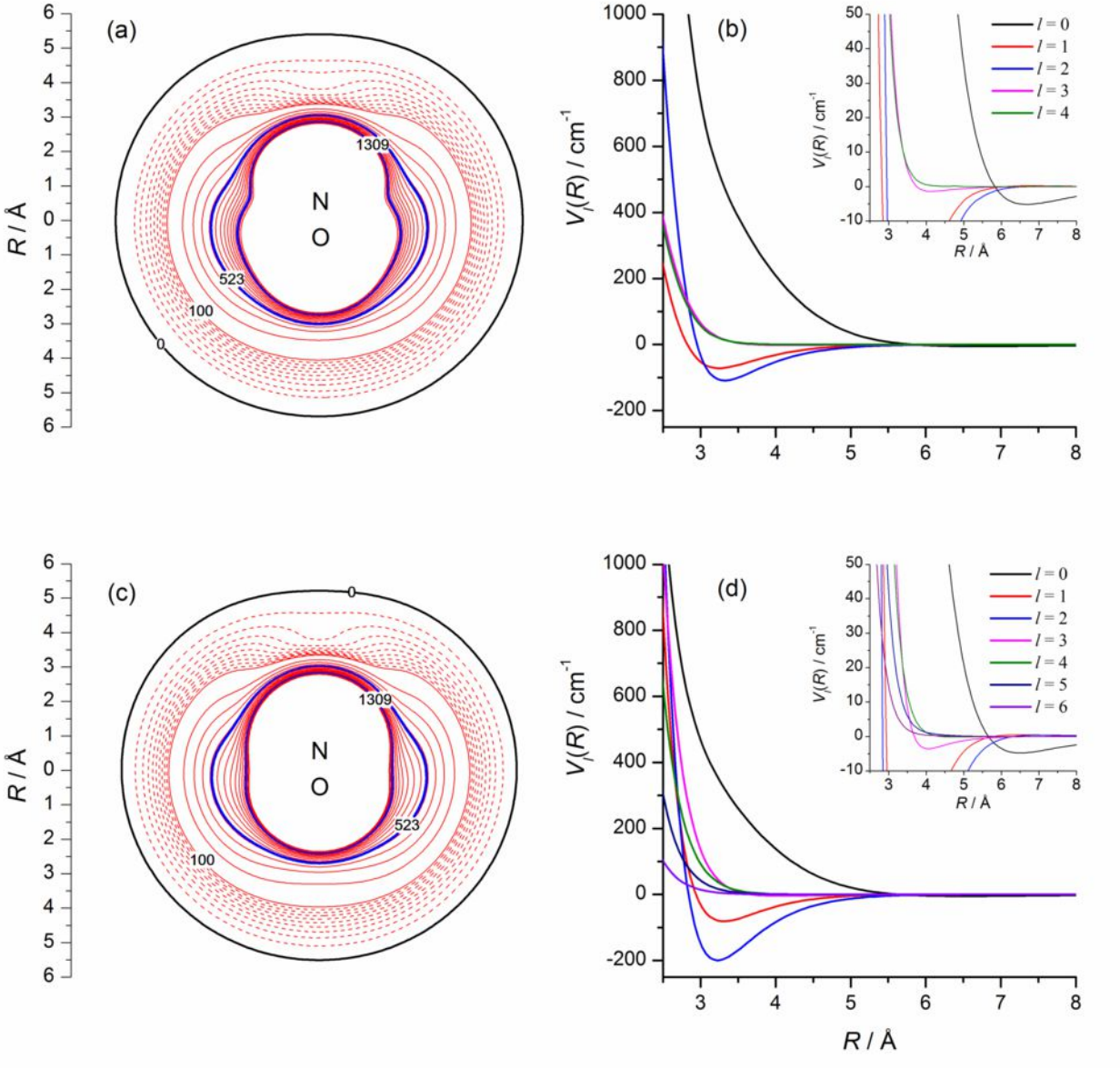
(a)
(b)
(c)
(d)
R / Å
N
O
1309
523
100
0
V_l(R) / cm^-1
l = 0
l = 1
l = 2
l = 3
l = 4
l = 5
l = 6

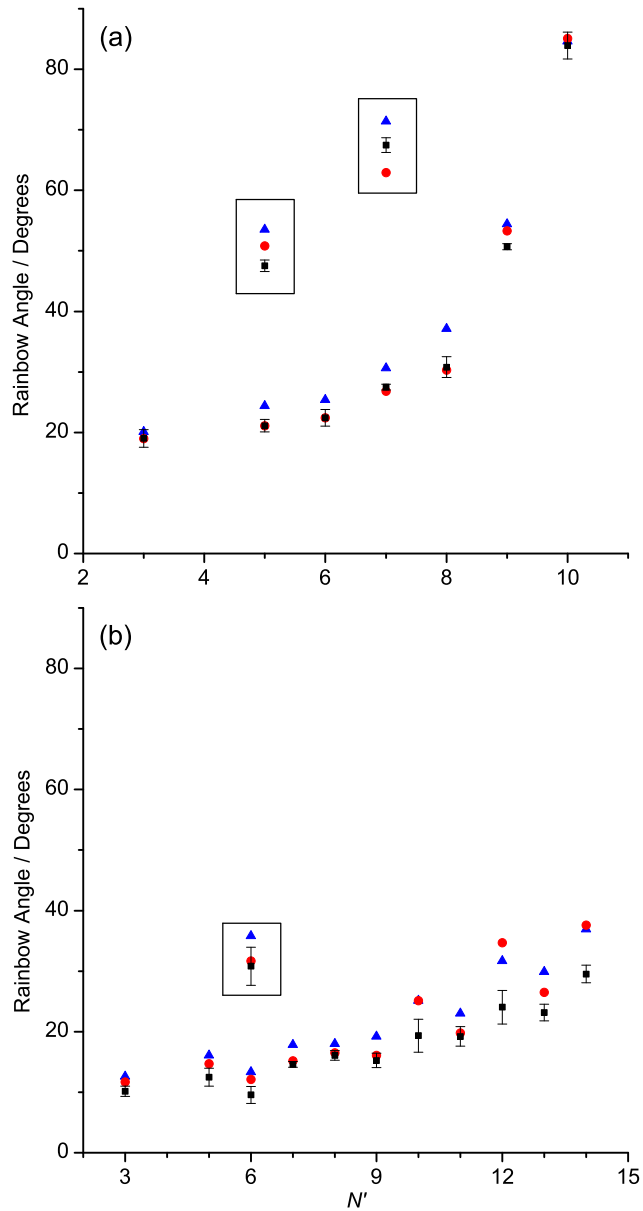
(a)
Rainbow Angle / Degrees
0
20
40
60
80
2
4
6
8
10
(b)
Rainbow Angle / Degrees
0
20
40
60
80
3
6
9
12
15
N′

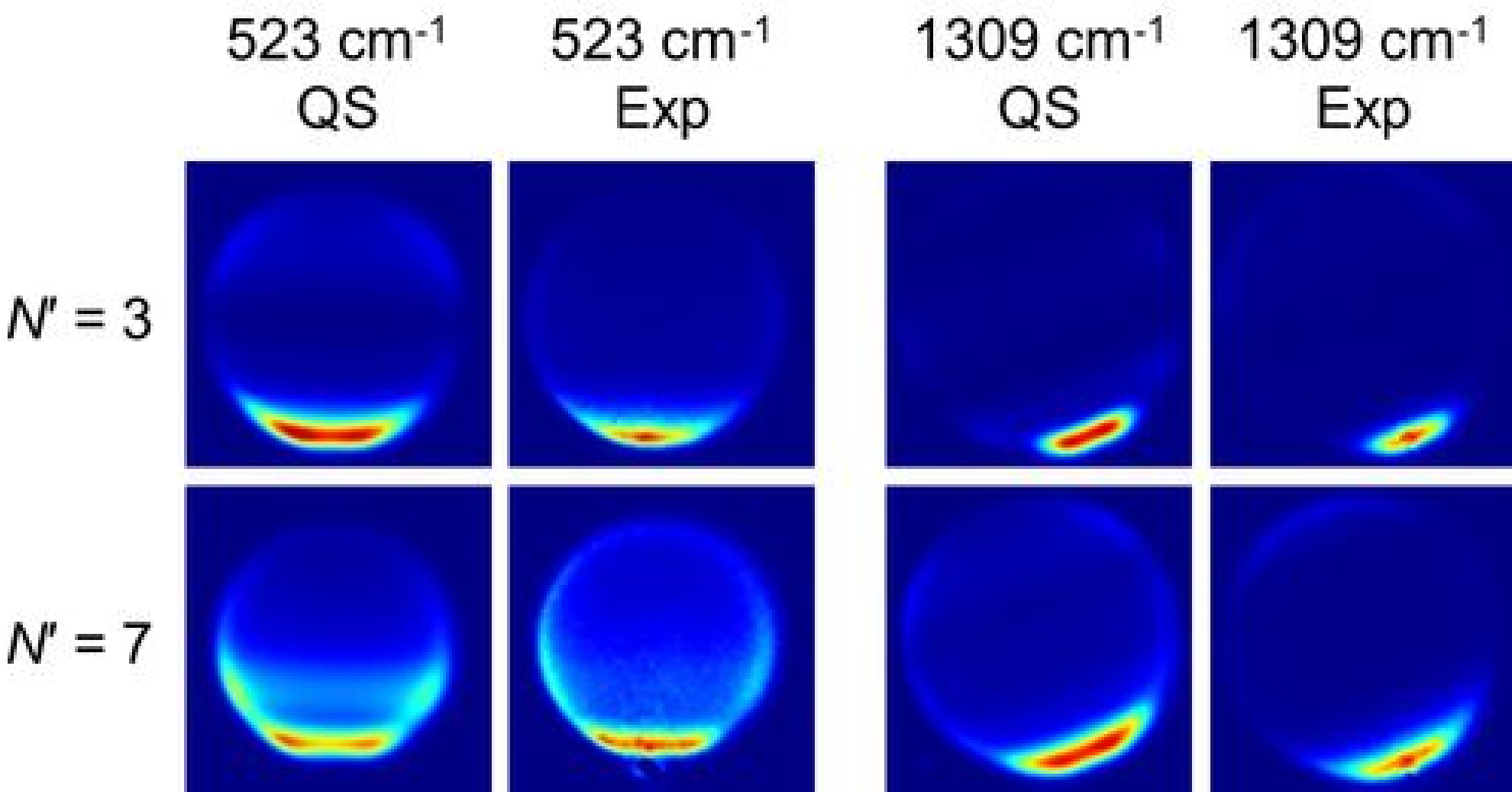
523 cm-1
QS
523 cm-1
Exp
1309 cm-1
QS
1309 cm-1
Exp
N′ = 3
N′ = 7